JOURNAL OF MATERIALS SCIENCE 12 (1977) 1927–1949

Review

Current views on the structure and crystallization of metallic glasses

Y. WASEDA*, H. OKAZAKI†, T. MASUMOTO‡
X-ray Diffraction Laboratory, The Research Institute of Mineral Dressing and Metallurgy, Tohoku University, Sendai 980, Japan

An attempt has been made in this review to cover recent information on the structure of metallic glasses (amorphous metals) obtained by X-ray diffraction. Based on the experimental data, the partial structure factors of a binary metallic glass are given. Various characteristics such as crystallization processes, thermal effects and alloying effects are also discussed.

1. Introduction

Recently, a large number of metallic glasses have been obtained by several techniques of quenching from the liquid state and their structure and properties have been studied. Many of these studies are reported in previous reviews [1–8], but recent progress in the structural study of metallic glasses is not yet covered. Since metallic glasses are thermodynamically unstable, transformation to stable crystalline phases should occur during heating and hence the crystallization process is one of the most important problems in the study of metallic glasses. Recently, it has been found that distinct changes in some properties related to the structure are induced by heating, even at temperatures appreciably lower than the so-called crystallization temperature. The main purpose of this paper is to review this new information on the structure and crystallization processes of metallic glasses.

2. Analysis of X-ray diffraction data

X-ray diffraction has been frequently used to determine the structure of metallic glasses. The two techniques of transmission and reflection are generally employed. There are many techniques for the analysis of the measured X-ray intensity, and significant technical progress has been made, much of which is already reviewed [1, 4–6] and needs no description here. For convenience of discussion, however, the essential equations are given below.

Assuming the disordered materials, amorphous and liquid, to have a continuous distribution of atoms, the intensity of coherent X-ray scattering per atom expressed in electron units $I_{eu}^{coh}(Q)$, which is directly obtained experimentally from more than one kind of atom, can be written as

$$I_{eu}^{coh}(Q) = \langle f^2 \rangle + \langle f \rangle^2 \int_0^\infty 4\pi r^2 [\rho(r) - \rho_0] \frac{\sin(Qr)}{Qr} \, dr \quad (1)$$

where $\langle f^2 \rangle = \Sigma_i c_i f_i^2$, $\langle f \rangle = \Sigma_i c_i f_i$, c_i and f_i are the concentration and atomic scattering factor of the ith kind atom, $\rho(r)$ is the radial density function and ρ_0 is the average density of atoms. As the total interference function, or structure factor, $S(Q)$ is defined in the following form,

$$S(Q) = [I_{eu}^{coh}(Q) - \langle f^2 \rangle + \langle f \rangle^2] / \langle f \rangle^2, \quad (2)$$

*Present address: Department of Metallurgy and Materials Science, University of Toronto, Toronto M5S 1A4, Canada.
†Permanent address: The College of General Education, Niigata University, Niigata 950–21, Japan.
‡Permanent address: The Research Institute for Iron, Steel and Other Metals, Tohoku University, Sendai 980, Japan.

the atomic radial distribution function $4\pi r^2\rho(r)$ is evaluated by Fourier transformation from the data for $S(Q)$ in the following equation,

$$4\pi r^2\rho(r) = 4\pi r^2\rho_0 + \frac{2r}{\pi}\int_0^\infty Q[S(Q)-1]\sin(Qr)\,dQ. \quad (3)$$

The pair distribution function $g(r) = \rho(r)/\rho_0$ is also frequently used to discuss the structure of metallic glasses and liquids. In a binary alloy, the total interference function $S(Q)$ is also expressed by the three partial interference functions $S_{\alpha\beta}(Q)$ in the following form;

$$S(Q) = w_{ii}S_{ii}(Q) + w_{jj}S_{jj}(Q) + 2w_{ij}S_{ij}(Q) \quad (4)$$

where $w_{\alpha\beta} = c_\alpha c_\beta f_\alpha f_\beta/\langle f\rangle^2$. The partial interference function $S_{\alpha\beta}(Q)$ is defined by the generalized equation,

$$S_{\alpha\beta}(Q) = 1 + \frac{4\pi\rho_0}{Q}\int_0^\infty r\,[g_{\alpha\beta}(r)-1]\sin(Qr)\,dr \quad (5)$$

where $g_{\alpha\beta}(r)$ is the average distribution of β-type atoms found at a radial distance r from an α-type atom at the origin.

As shown in Equation 4, the structure of an i–j binary disordered alloy obtained directly from diffraction experiments is characterized by the three partial interference functions corresponding to the two like atom pairs (i–i and j–j) and the unlike atom pair (i–j). Separation of these individual interference functions is one of the important recent reports on it [9–13].

Recently, the X-ray anomalous scattering technique has also been used in this field. The fundamental relations of this technique were given by Ramesh and Ramashan in 1971 [14, 15], and the first application was carried out by Waseda and Tamaki (1975) [16]. This technique can give information supplementary to the results obtained by the common X-ray and neutron diffraction measurements as well as the isotope enrichment [17] and polarized neutron technique [9–11]. For convenience of discussion, the essential features of the X-ray anomalous scattering technique will be given below.

It is well-known that when the anomalous scattering of X-ray occurs, the total scattering factor becomes complex in the following form [18],

$$f_i = f_i^0 + \Delta f_i' + i\Delta f_i'', f_j = f_j^0 + \Delta f_j' + i\Delta f_j'', \quad (6)$$

where f_i^0 and f_j^0 correspond to the atomic scattering factor for radiation with frequency much higher than any absorption edge and $\Delta f'$ and $\Delta f''$ are the real and imaginary components of the anomalous dispersion term [19, 20]. Using this relation, the Laue monotonic scattering term in

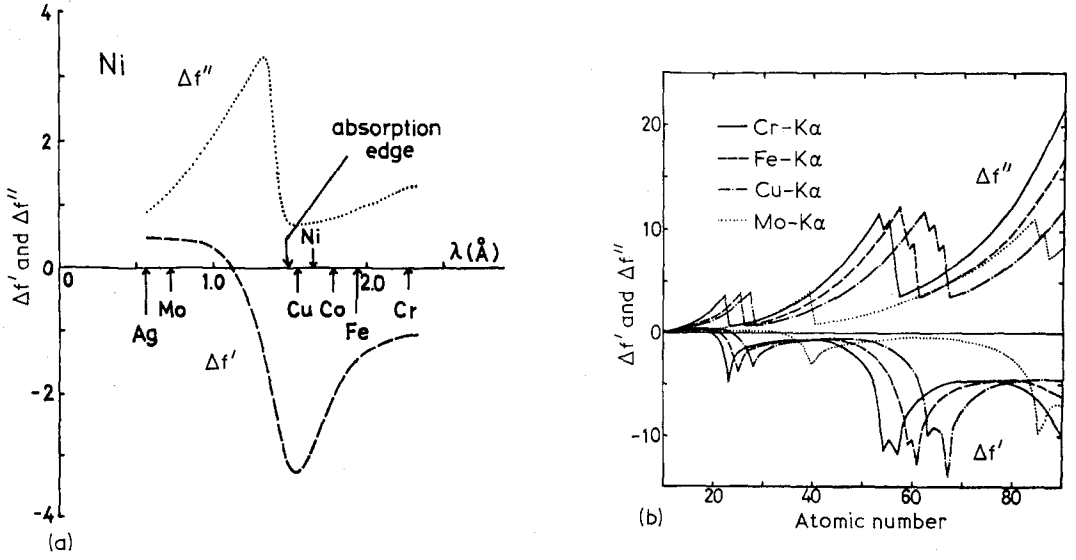

Figure 1 Anomalous dispersion terms $\Delta f'$ and $\Delta f''$ [19, 20]. (a) wavelength dependence of Ni atom. (b) correlation with atomic number.

Equation 2, $(\langle f^2\rangle - \langle f\rangle^2)$, and the weighting factor $w_{\alpha\beta}$ in Equation 4 may be written as follows,

$$(\langle f^2\rangle - \langle f\rangle^2) = c_i(1-c_i)f_i^* f_i + c_j(1-c_j)f_j^* f_j - 2c_i c_j[(f_i^0 + \Delta f_i')(f_j^0 + \Delta f_j') + \Delta f_i'' \Delta f_j''], \quad (7)$$

$$w_{ii} = c_i^2 f_i^* f_i / \langle f\rangle^2 \quad \text{and} \quad w_{jj} = c_j^2 f_j^* f_j / \langle f\rangle^2, \quad (8)$$

$$w_{ij} = c_i c_j [(f_i^0 + \Delta f_i')(f_j^0 + \Delta f_j') + \Delta f_i'' \Delta f_j'']/\langle f\rangle^2 \quad (9)$$

The anomalous dispersion terms $\Delta f'$ and $\Delta f''$ are dependent on the wavelength of the incident radiation as shown in Fig. 1a using the Ni atom as an example. The wavelengths of Cu$K\alpha$ and Co$K\alpha$ radiation are located near an absorption edge of Ni atoms, so that measurement of the X-ray scattering intensity at two wavelengths near the absorption region give two additional items of information concerning the total structure of a binary alloys. These data, when coupled with those obtained from normal measurements using the wavelengths away from the absorption edge region (Mo$K\alpha$ in Fig. 1a), permit the separation of the three partial structures. As shown in Fig. 1b, the anomalous dispersion terms for several radiations indicate discontinuous variation with the atomic number. Consequently this technique is applicable to alloys of 3d transition metals or lanthanide elements.

3. Experimental structure data for various metallic glasses

3.1. General features

Schematic diagrams for the typical states of a gas, liquid, amorphous material and a crystal are shown in Fig. 2. In the gaseous state, atoms are distributed with a low average density and a mean free path that is long compared with the atomic size. In both the liquid and amorphous states, the atoms are randomly distributed in a nearly close-packed

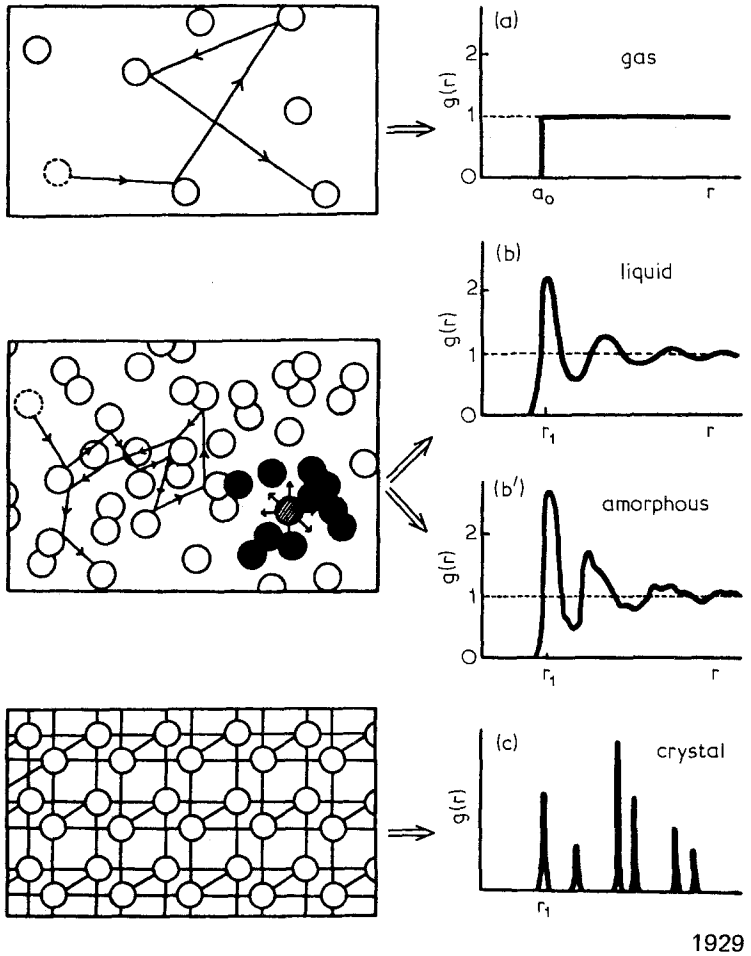

Figure 2 Schematic diagrams of atomic distributions in the gas, liquid, amorphous and crystal states [6].

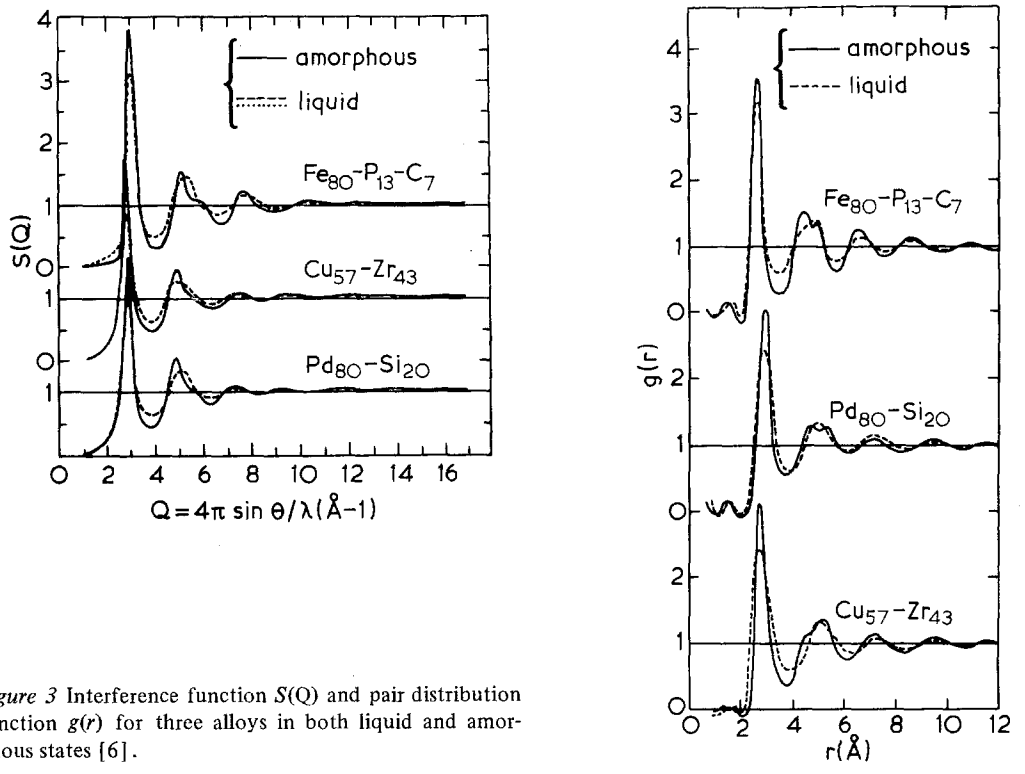

Figure 3 Interference function $S(Q)$ and pair distribution function $g(r)$ for three alloys in both liquid and amorphous states [6].

structure, with a short mean free-path, comparable with the atomic size; the co-ordination number of nearest neighbour atoms is about 10 in both cases. But the average atomic configurations in the liquid state are more homogeneous than those of the amorphous state when averaged over time and space because of the relatively high atomic mobility. In other words, the atomic configurations in the amorphous state are more rigid compared with those of the liquid state. This means that the average atomic distributions in the amorphous state may show slight inhomogeneities. In the crystalline state, the atoms occupy the cube corners of a regular three dimensional lattice. Reflecting these characteristics, the respective pair distribution functions $g(r)$ are shown schematically on the right hand side of Fig. 2, where a_0 is the atomic hard core.

Based on this simple and qualitative discussion, the experimental results for liquid and amorphous metals are investigated below. A comparison between the structure of the amorphous state and that of the liquid state is shown in Fig. 3 for three typical metallic alloy glasses [6]. (These amorphous metals are prepared by rapid quenching from the melt). As is seen in Fig. 3, the general features of the structure of the amorphous state is similar to that of the liquid state except for a shoulder on the second peak observed in both $S(Q)$ and $g(r)$. As a more simple case, Fig. 4 shows the structural data for amorphous [21] and liquid Ni [22]. (In this case the amorphous sample was prepared by vapour quenching). The clear difference between the structure of amorphous Ni and that of liquid Ni is demonstrated by the splitting of the second peak.

The ratio of the peak positions in real space, as obtained from the pair distribution functions for some transition metals are listed in Table I. The

TABLE I Peak ratio in the pair distribution function for transition metals in amorphous and liquid states.

Metal	Amorphous		Reference	Liquid*	
	r_2/r_1	r_3/r_1		r_2/r_1	r_3/r_1
Cr	1.66	1.91	[25]	1.85	2.68
Mn	1.67	1.96	[25]	1.86	2.72
Fe	1.67	1.90	[21]	1.85	2.73
	1.67	1.96	[25]		
Co	1.65	1.90	[23]	1.87	2.73
	1.69	1.93	[25]		
Ni	1.71	1.93	[21]	1.86	2.71
	1.65	1.90	[23]		

* Waseda and Tamaki [22]

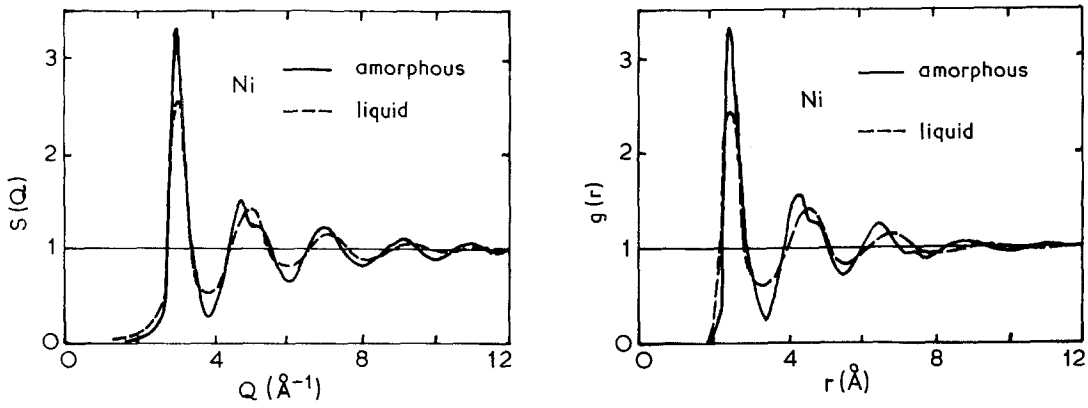

Figure 4 Comparison between the structure of amorphous Ni [21] and that of liquid Ni [22].

ratio (r_2/r_1) of the position of the first peak (r_1) to that of the second peak (r_2) in the amorphous state is nearly equal to the constant value of about 1.67; in the case of the third peak, this is about 1.95. In contrast with these results, the ratios are 1.85 and 2.70, respectively, in the liquid state. These relations remain the same in the alloy systems as shown in Table II. The ratio $(r_2/r_1) = 1.67$ in the amorphous state is close to the mean value between the c/a ratio in close-packed hexagonal structure (i.e. $c/a = 1.63$), and the ratio of the third atomic shell radius to the nearest neighbour distance in fcc structure (i.e. $\sqrt{3} = 1.73$). This implies that the short range order of near neighbours in the amorphous state is affected more or less by the atomic arrangement of crystalline state. However, from the similarity of the gross features of $S(Q)$ and $g(r)$, the fundamental configuration of atoms seems to be liquid-like.

At the present time we have two models for the disordered structure. One is the microcrystalline disorder model and the other is the topological disorder model. The microcrystalline disorder model is frequently used to discuss the structure of amorphous metals. In it, small crystallites are considered to be randomly distributed, and the inhomogeneity of atomic configuration in the boundary regions is not considered. A more realistic form is the combination of small crystallites and boundary regions as shown schematically in Fig. 5. On the other hand, the topological disorder model is based on certain fundamental units (see, bottom of Fig. 5): the smallest unit is the tetrahedron, corresponding to the smallest form of a close-packed structure such as the fcc or hcp type. In this model these units are irregularly and continuously arranged. This type of model structure is also called the dense random packing model and is based on the concept proposed by Bernal in 1959 for liquids. An analytic formulation of this model is not possible, so that concrete results are given only for a computer model similation for about 1000 particles; this is the disadvantage of the topological disorder model.

TABLE II Peak ratio in the pair distribution function for various alloy systems in amorphous and liquid states.

Alloy system	State	r_2/r_1	r_3/r_1
$Pd_{80}-Si_{20}$	amorphous	1.67	1.88
	liquid	1.86	
$Cu_{57}-Zr_{43}$	amorphous	1.70	1.89
	liquid	1.87	
$Fe_{80}-P_{13}-C_7$	amorphous	1.66	1.92
	liquid	1.86	
$Ni_{80}-P_{20}$	amorphous	1.66	1.87
	liquid	1.85	
$Fe_{78}-Si_{10}-B_{12}$	amorphous	1.69	1.91
$Co_{78}-Si_{10}-B_{12}$	amorphous	1.67	1.89
$Ni_{78}-Si_{10}-B_{12}$	amorphous	1.66	1.89

Fig. 6 shows the results for an amorphous $Ag_{48}-Cu_{52}$ alloy reported by Wagner and coworkers [27], the amorphous sample being prepared by vapour quenching. The amorphous structure is in good agreement with that calculated from the microcrystalline disorder model, but as is seen in this figure, the pattern for this type of structure differs from the typical patterns of amorphous metals and it seems that in general, the structure of amorphous metals can be approximated to the topological disorder model in contrast to the microcrystalline disorder model.

The results of the hard sphere model for liquids, the so-called hard sphere solution of the

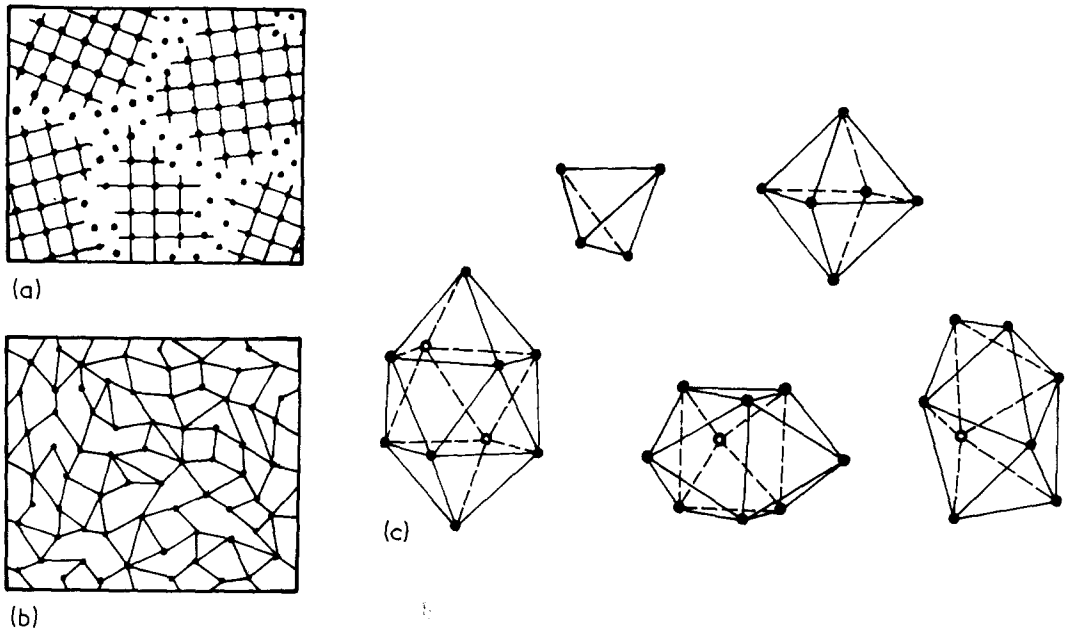

Figure 5 Schematic diagrams of models for the disordered structure: (a) microcrystalline disorder model, (b) topological disorder model, (c) idealized holes described by Bernal [65] to express the topology of dense random packing.

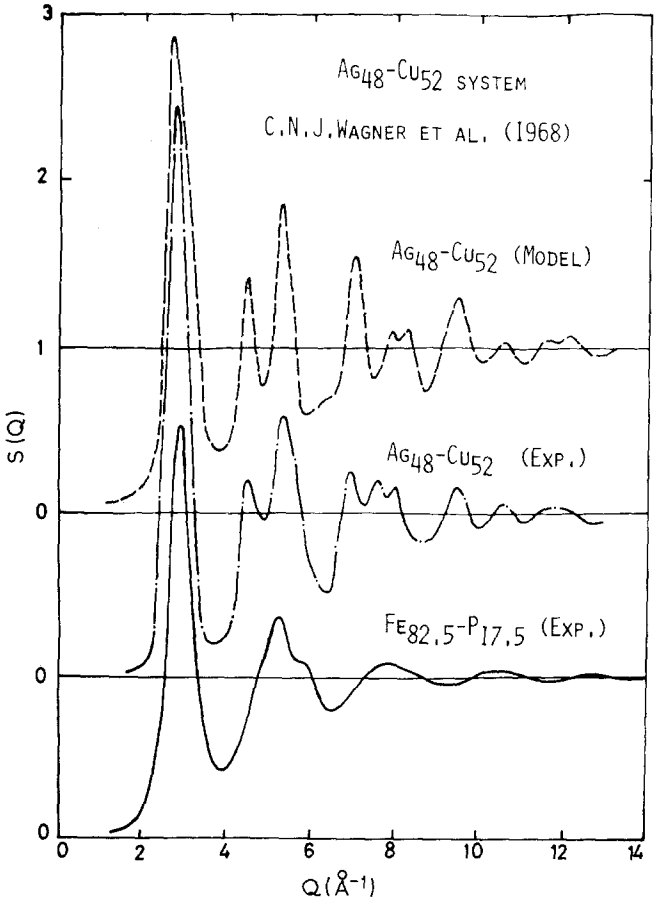

Figure 6 Structure of amorphous $Ag_{48}-Cu_{52}$ alloy [27] and $Fe_{82.5}-P_{17.5}$ alloy [32].

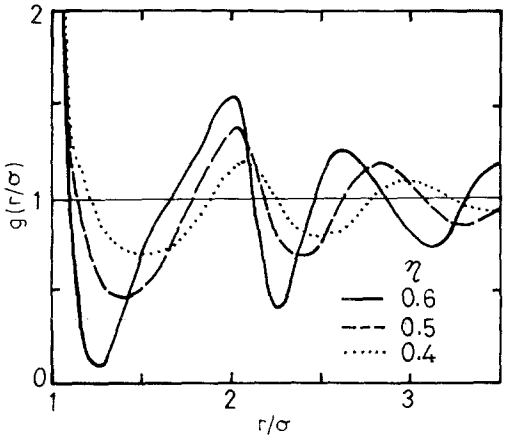

Figure 7 Model structure of hard spheres at various packing density η using the Percus–Yevick equation for liquid structures.

Percus–Yevick equation, are shown in Fig. 7. The peak maxima become sharp and the distortion of the second peak is found to increase with increasing packing density, η. But the hard sphere model of liquids never reproduces the characteristic splitting of the second peak seen in the amorphous structure for the case of higher packing density. Hence in a discussion of amorphous structure the simple model structure of hard sphere liquids of Fig. 7 is not necessarily sufficient. A more rigid configuration of atoms is considered in the topological disorder model, and it is shown that there is a relation between the atomic distribution in liquids and that in the model [6]. Fig. 8 show a schematic diagram for the fundamental configuration of atoms in the random liquid-like distribution [66]. In this distribution, taking atom O as the centre atom, A is at a distance approximately equal to the first nearest neighbour distance r_1. Of course at the same distance r_1 from atom A, we find other atoms such as D, E, F and so on; about 10 atoms on average. Atom O is fixed in these configurations, but atom F is not on the lattice point of the close-packed f c c structure, because the atoms continuously vibrate within the region of root mean square displacement about lattice point (the shaded region in this figure). Therefore, the distance of the second nearest neighbouring atoms is between 1.6 and 1.9 times the nearest neighbour distance r_1. In the liquid state, the amplitude of atomic vibration is large and so the uncertainty in the position of the lattice point is also rather large and the second nearest neighbour position approximates to an average value between 1.6 r_1 and 1.9 r_1. The small amplitude of vibration of atoms such as those in the amorphous state leads to a more fixed atomic arrangement still having, however, the characteristics of a random distribution, and two peak positions (1.6 r_1 and 1.9 r_1) may be observable in the second peak. If the atoms occupy the positions E and F, which are the centre positions of the triangles ABD and BCD in the side of the tetrahedron ABCD, the distances AF, CE and EF are nearly equal to a value about 1.6 the nearest neighbour distance r_1. From this, the shorter distance of 1.6 r_1, found in the instantaneous atomic distribution of liquid-like structures, just corresponds to the distance in the topological disordered structures [5, 6].

Consequently, the amorphous structure seems to involve tetrahedra as the fundamental units of a close-packed disordered atomic distribution and is relatively distinct in comparison with that of liquids. In other words, the packing of tetra-

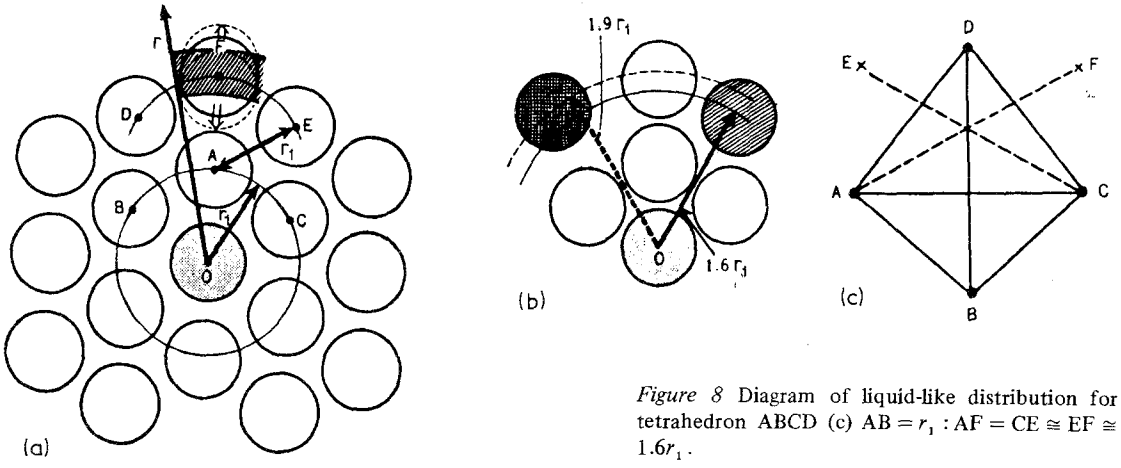

Figure 8 Diagram of liquid-like distribution for tetrahedron ABCD (c) AB = r_1 : AF = CE ≅ EF ≅ 1.6r_1.

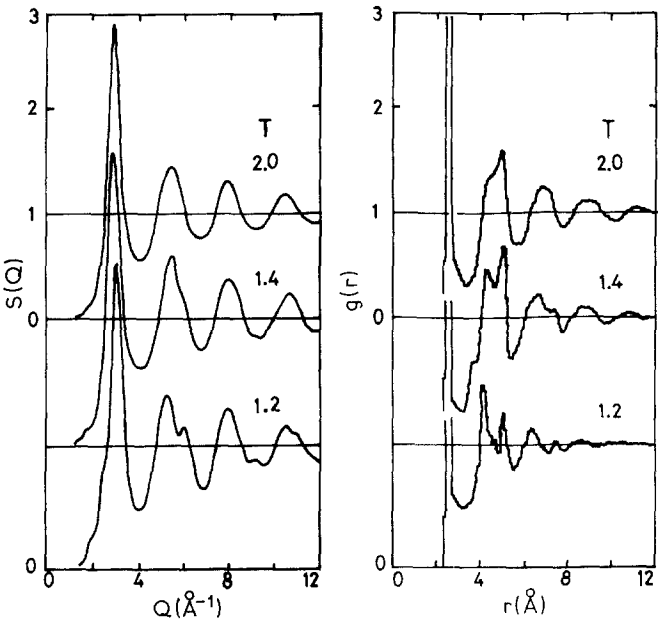

Figure 9 Results for dense random packing of hard spheres [28].

hedrons in the amorphous state is relatively rigid, whereas in the liquid state this packing becomes obscure. This speculation is quantitatively supported by a recent model calculation [28, 29]. Fig. 9 shows, for example, the results of Ichikawa (1975). In his calculation, the case of the parameter $T = 1.2$ corresponds to the rigid packing of tetrahedrons. In this case the splitting of the second peak in both $S(Q)$ and $g(r)$ is clearly demonstrated and this is in good agreement with the experimental data of Figs. 3 and 4. But the packing becomes obscure for $T = 2.0$, that is, the fundamental tetrahedra are distorted; the splitting of the second peak is no longer observed, which is also in good agreement with the experimental results for the liquid state.

To summarize, the amorphous structure is expressed, to a first approximation, by the more rigid packing of the tetrahedral units than in the case of liquids. It should be borne in mind that the atomic configuration consists of mainly disordered distributions in both the amorphous and liquid states with the tetrahedron as the fundamental unit.

3.2. Structural disorder parameter

In the field of structural studies of amorphous alloys, the structural disorder seems to be one of the most important parameters. However, no definite answer to this problem is available at present. Consequently, using the experimental data of the pair distribution function, a semi-empirical approach [30, 31] for estimating the region of short range order is given below. We employ r_s [1], the range of r beyond which the short-range order disappears and where $g(r) = 1 \pm 0.02$. The fluctuation of ± 0.02 is considered to be reasonable from considerations of errors in $g(r)$ at large r. This assumption implies that a large value of r_s corresponds to the extended ordering domain, where the atomic configurations deviate from the average density. In extreme cases, r_s is infinite in the crystalline state and equal to the nearest neighbour distance in the gaseous state. A similar approach is also discussed in a previous review [1], although there are differences in detail. In this paper, a dimensionless parameter for the structural disorder, involving r_s, is defined as

$$\zeta = r_s/r_1 \tag{10}$$

where r_1 is the nearest neighbour distance. Table III shows the parameter ζ for various alloys estimated from the experimental data. As shown in the table, the value for amorphous alloys is ~ 5.7 and this is larger than that (~ 4.2) for the liquid state. The results in the table also indicate that the parameter for amorphous alloys is independent of the alloy composition. Therefore, it is expected that when the amorphous samples have ζ of the same order, their structural disorder may be quite similar.

TABLE III Disorder parameter ζ estimated from experimental structural data for various alloys in amorphous and liquid states.

Alloy/state	r_1 (Å)	r_s (Å)	ζ
$Pd_{80}-Si_{20}$			
amorphous	2.81	16.0	5.96
liquid	2.76	11.5	4.17
$Fe_{80}-P_{13}-C_7$			
amorphous	2.58	15.0	5.81
liquid	2.58	11.0	4.26
$Ni_{80}-P_{20}$			
amorphous	2.55	14.0	5.49
liquid	2.53	10.5	4.15
amorphous			
$Fe_{78}-Si_{10}-B_{12}$	2.58	15.0	5.81
$Co_{78}-Si_{10}-B_{12}$	2.53	14.5	5.73
$Ni_{78}-Si_{10}-B_{12}$	2.55	14.5	5.69
liquid			
Fe	2.58	10.5	4.07
Co	2.56	11.0	4.30
Ni	2.53	10.5	4.15

3.3. Partial structures

In this section, the recently obtained partial structures for binary metallic glasses will be reviewed and discussed.

Fig. 10 shows a comparison of the results obtained by X-ray anomalous scattering techniques with those obtained by the polarized neutron technique for amorphous Co–P alloys [9]. The vertical lines in Fig. 10b denote the difference due both to alloy composition and to the residual uncertainty of experimental errors, which are $\sim \pm 0.3$. This implies that the differences in alloy composition lead to changes in the resulting partial structures which are not severe for amorphous Co–P alloys. This is also found for amorphous Ni–P [12], Fe–P [32], and Cu–Zr [33] alloys. In both sets of results, obtained independently by the different techniques, the encouraging agreement is worthy of note, although there are differences in detail.

Figs. 11 and 12 are the results for amorphous Ni–P and Cu–Zr alloys [13, 33]. It is well-known that the analysis by X-ray anomalous scattering and polarized neutron techniques is restricted to about $Q = 7.0$ Å^{-1}, and the spurious ripples in $g_{ij}(r)$ due to the finite termination of $S_{ij}(Q)$ cannot be removed even though quite accurate data for $S_{ij}(Q)$ are used. It is relatively easy, however, to trace the positions where the spurious ripples appear significantly. According to Finbak (1949) [34] and Sugawara (1951) [35], the oscillation appears at $\Delta r \simeq \pm 5\pi/2Q_{max}$ or $\pm 9\pi/2Q_{max}$ from the principal peak position, where Q_{max} is the experimentally observed upper limit of Q. This check is important in the case of P–P pairs. The arrows in Fig. 12 indicate the assumed positions of these spurious ripples. The peak at ~ 1.9 Å in the pair distribution function of the P–P pairs seems to be a spurious one as well as those at ~ 1.0 and 5.2 Å, although the corresponding spurious peak at 4.2 Å is not distinctly observed in Fig. 12. Therefore it may be reasonable to say that the peak in the pair

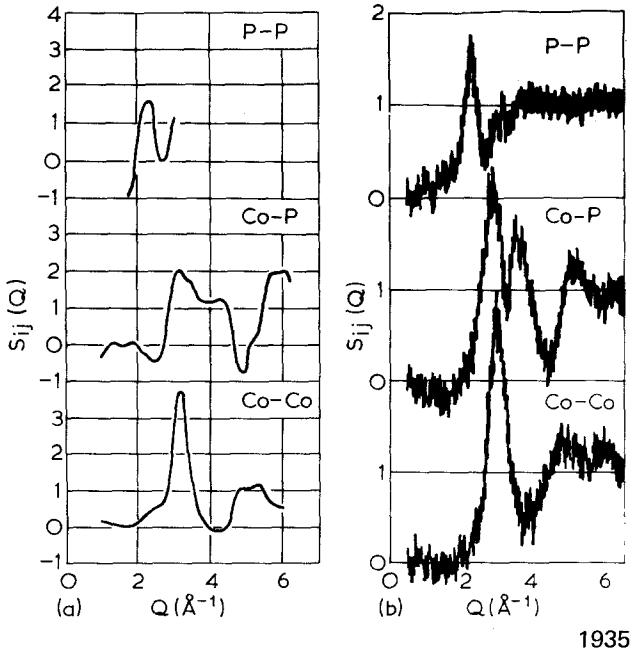

Figure 10 Partial interference function $S_{\alpha\beta}(Q)$ of amorphous Co–P alloys; (a) polarized neutron technique [9], (b) X-ray anomalous scattering technique [14–16].

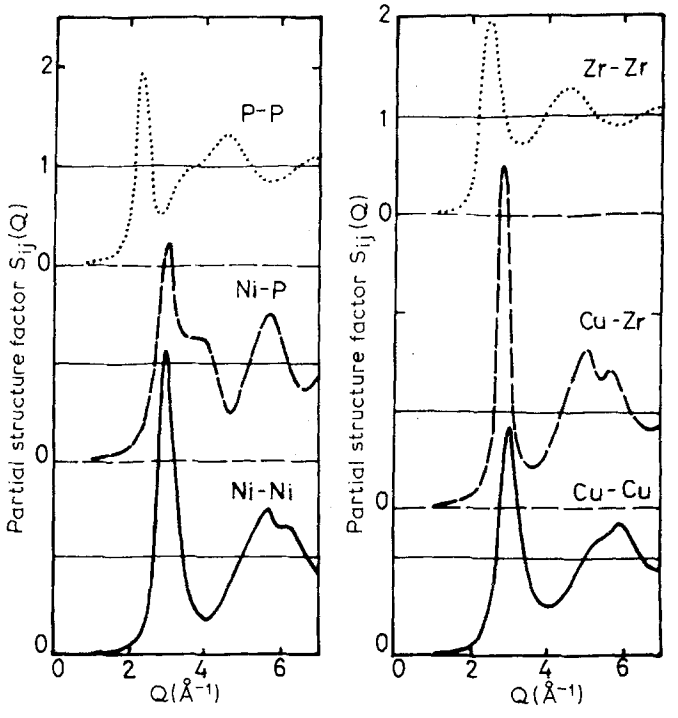

Figure 11 Partial interference function $S_{\alpha\beta}(Q)$ of amorphous Ni–P and Cu–Zr alloys [13, 33].

distribution function for P–P pairs at $\sim r = 3.1$ Å is a significant one so that P atoms are never at the first nearest neighbour distance. This result would indicate that the short range order of nearest neighbours in amorphous Ni–P alloys seem to be of a Ni_3P type structure. As shown in Table IV, this proposal is easily checked by considering correlation of atoms in the near neighbour positions derived from these partial structural data. But it should be kept in mind that the amorphous Ni–P alloys are not composed of small Ni_3P crystallites; this is a coincidence between the experimental and the model calculations. If this definite configuration of atoms existed, structures such as those observed in amorphous Ag_{48}–Cu_{52} alloy (see Fig. 6) should be found. On the other hand, as shown in the previous section, the topological disordered structure is applicable to amorphous metals. From these results, we suggest that the atomic distributions in the amorphous Ni–P alloys consist mainly of randomly distributed Ni atoms like those in the dense random packing model based on tetrahedral units. The P atoms occupy the vacant spaces in this distribution of Ni atoms. However, a deformed crystalline-like characteristic may partly contribute to the short range order in amorphous alloys (see Section 3.1). The authors hold the view that this crystalline-like configuration of atoms is not the same exact arrangement as in the crystalline state already discussed by Cargill and Cochrane [37]. Structural information of this type is also reported in the amorphous systems of Co–P [9, 11, 38], Ni–P [13] and Pd–Si [39, 40]. As is easily predicted from the size factor of transition metal and metalloid elements, the expansion of the metal–metal atom distance is unavoidable in the configurations of the above type. This is supported by the results in Fig. 13. There is an interesting point in these results, namely that the size factor difference of constituent elements in all of these alloys is more than 15%. This is also true for the typical amorphous system of Pd–Si. On the other hand, as shown in Fig. 13, such expansion is not observed in either liquid Fe–Si or Ni–Si alloys [41]. In these systems, the size factor dif-

TABLE IV Comparison between the correlation of atoms in the near neighbour region for amorphous Ni–25 at. % P alloy with that of crystalline Ni_3P

		Ni		P	
	Origin atom	r (Å)	n (atoms)	r (Å)	n (atoms)
Amorphous Ni–P alloy	Ni	2.55	10.7	2.35	2.2
	P	2.35	8.5	3.30	3.6
Crystalline Ni_3P*	Ni	2.68	10	2.28	3
	P	2.28	9	3.44	4

*Rundquist *et al.* [36]

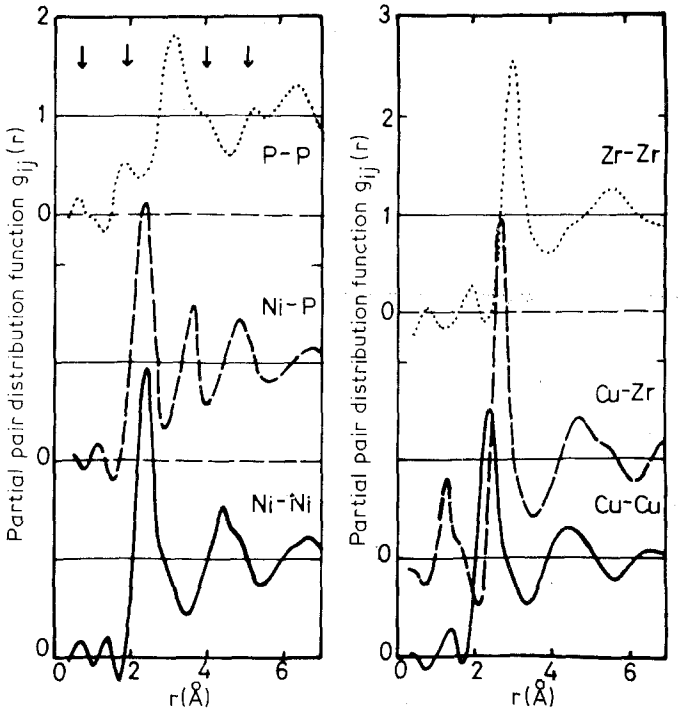

Figure 12 Partial pair distribution function $g_{\alpha\beta}(r)$ of amorphous Ni–P and Cu–Zr alloys [13, 33].

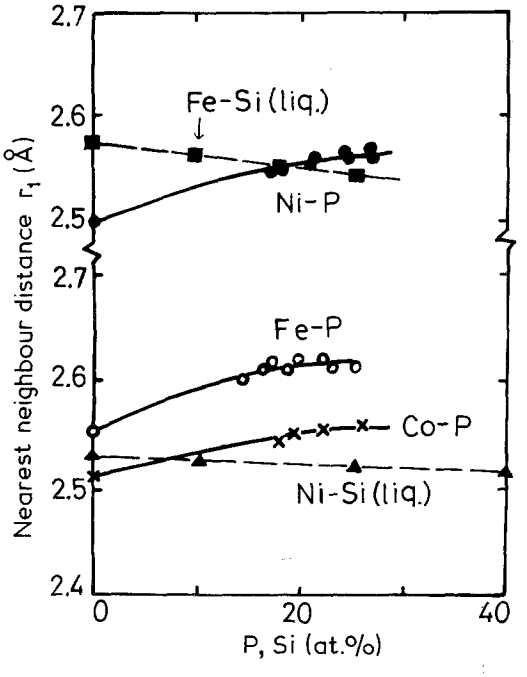

Figure 13 Change of nearest neighbour distance as a function of the concentration of P atoms in amorphous transition metal–phosphorous alloys. Co–P [37], Fe–P [32, 49], Ni–P [5, 13].

ference is about 7%. The amorphous phase is not observed in Fe–Se and Ni–Si alloys by using the common centrifugal or roller quenching techniques, contrary to the results of vapour deposition. The kinetic effects [24], chemical bonding or electron transfer effects [26] between constituents of the alloys also play a important role in the formation of amorphous phase. But the characteristic in Fig. 13, together with the same order of difference in size factor in amorphous metal–metalloid systems must be one of the interesting factors of amorphous phase formation, because the phosphorous-containing alloys are easy glass formers. Nevertheless no quantitative conclusion regarding size factor effects is available at the present time.

Although it has been generally accepted that glass-forming alloys include a metalloid as one of the constituents, more recently several exceptions have been found in alloy systems consisting of two metallic elements. A comparison therefore, of the structure of a metal–metalloid system with that of metal–metal systems is given below.

Fig. 11 shows the partial structure factors $S_{ij}(Q)$ for Cu–Zr alloys evaluated from the measured intensity data, together with those for amorphous Ni–P alloys. The obtained partial pair distribution functions $g_{ij}(r)$ are shown in Fig. 12.

The general features of the structure of amorphous Ni–P and Cu–Zr alloys are as follows:

(1) The form of the partial structure factors of two like atom pairs are similar to those observed in pure liquid Ni, Cu, Zr and P [22, 42, 43].

(2) The pre-maximum below the first peak

corresponding to compound formation or to long-range ordering is not found in any of the partial structure factors. Such ordering behaviour has been observed, for example, in an amorphous Cu–65 at.% Mg alloy [44].

(3) The first peak in the partial pair distribution function of Ni–Ni and Cu–Cu pairs is asymmetric where the left-hand side of the first peak is steeper than that of the right-hand side.

(4) The splitting of the second peak is observed in the partial structure factors of Ni–Ni and Cu–Zr pairs. Moreover, the third peak in the partial structure factor of Ni–P pairs lies in the region of the split second peak of the total structure factor, and in the case of Cu–Zr alloys the second peak of Zr–Zr pairs lies in this region. Such behaviour is also found in the pair distribution functions.

Feature (1) implies that the partial structure factors in these amorphous alloys are approximately independent of concentration within the measured composition range. Feature (2) indicates that the structure of these amorphous alloys is consistent with a more or less random mixture of two consistuent elements. (3) may correspond to a situation where the repulsive core part of the pair potential for Ni–Ni and Cu–Cu pairs is more vertical than the attractive part. (4) could be an indication that the distribution of unlike atom pairs and like atom pairs having the larger sphere diameter contributes mainly to the splitting of the second peak; one of the main differences in the structure of the amorphous and liquid states.

The above features apply to both alloy systems, i.e. metal–metalloid and metal–metal systems, but the following difference is found in the structural data: a curious peak in the partial structure factor of Ni–P pairs is clearly indicated, whereas this is not found in the partial structure factor of Cu–Zr pairs. This subsidiary peak is not reproduced by the dense random packing model [5]. A similar difference is found by comparing the structure of amorphous Tb–Fe alloys [10] and that of metal–metalloid systems. This behaviour related to the curious peak may therefore suggest that the detailed atomic distribution in amorphous metal–metalloid systems differs from that in amorphous metal–metal systems. As mentioned above, the atomic distributions in amorphous Ni–P alloys consist mainly of randomly distributed Ni atoms like those in the dense random packing model, in which the P atoms occupy the vacant space. On the other hand, the Cu and Zr atoms in amorphous Cu–Zr alloys act, to a first approximation, as liquid-like closely packed hard spheres. From these experimental results however one cannot make any definitive statements on the difference in the atomic distributions between the metal–metalloid systems and metal–metal systems because the fundamental unit in the short-range order of the liquid-like close-packed structure is the tetrahedron which also features in the topological disordered structure of dense random packing model. Consequently, no definite answer to the problem related to the subsidiary peak of metal–metalloid pairs is available at the present time.

3.4. A comparison between structures of oxide glass and metallic glass

So far as the author is aware, direct comparison between the structure of metallic glasses and that of typical conventional glasses such as oxide glasses has received little attention. In this section, the difference between oxide glasses and metallic glasses is examined in the light of recent experimental data. Fig. 14 shows the so-called pair distribution function $G(r)$, derived from measured intensity data by Fourier transformation, for SiO_2 [45–47] and $Fe_{82.5}$–$P_{17.5}$ alloy prepared by the liquid quenching method in the glassy state [32]. At first sight, the general forms of the first peak and subsequent small oscillations are similar. But the following interesting difference between the structures is found: the first peak of SiO_2 glass is very sharp and almost completely resolved and the

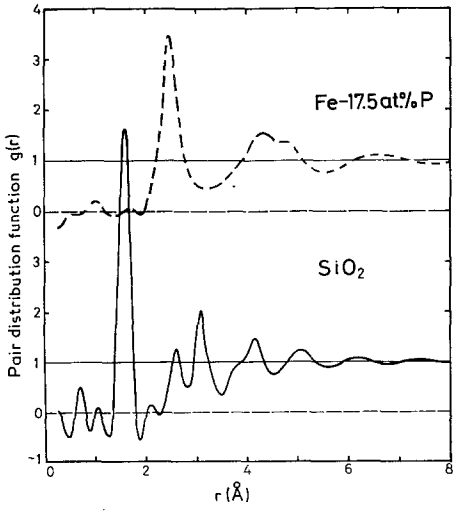

Figure 14 Pair distribution function of glassy SiO_2 and $Fe_{82.5}$–$P_{17.5}$ alloy [32].

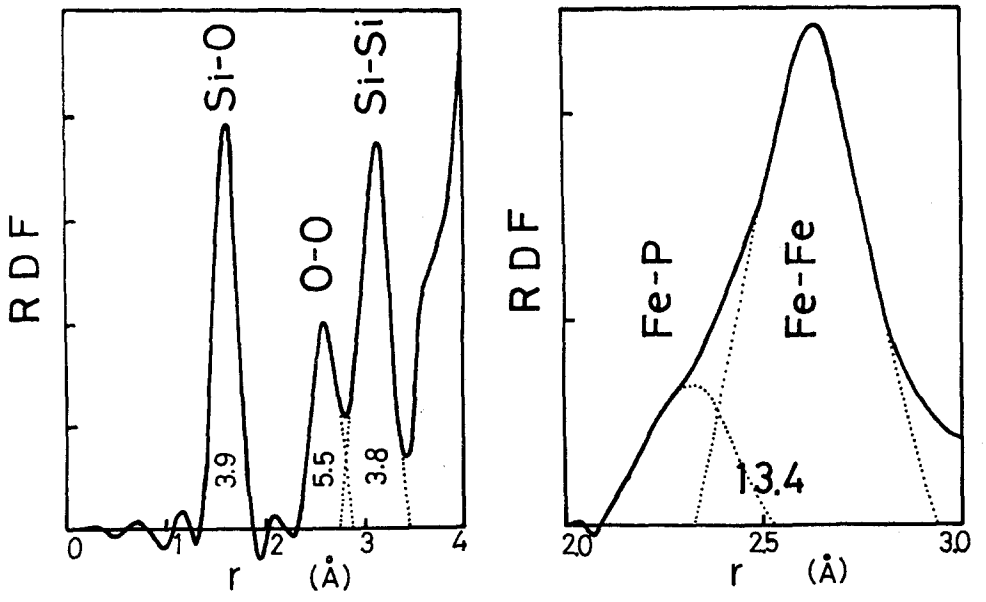

Figure 15 Pair distribution function of glassy SiO_2 and $Fe_{82.5}-P_{17.5}$ alloy [32].

oscillations decay rapidly, with the pair distribution function showing no structurally significant deviation from the asymptotic value of the average density $G(r) = 1$ at large r. This behaviour, observed in molecular liquids, corresponds to a distinct local nearest neighbour correlation. On the other hand this almost complete resolution of the first peak is not observed for the $Fe_{82.5}-P_{17.5}$ alloy glass, although the oscillations are well damped at large r. This observed difference in the first peak implies that the detailed structure of the SiO_2 glass differs from that of the Fe–P glass.

In order to reveal the ordering unit in these two types of glasses, the area under the respective peaks in the near neighbour correlation is estimated by the usual means. Fig. 15 shows the radial distribution functions and the near neighbour distances experimentally observed. The numerical values in this figure indicate the co-ordination number of the respective correlations estimated. As shown in these results, the near neighbour correlations in the SiO_2 glass are interpreted as the Si–O pairs completely resolved and the superposition of the correlations of O–O and Si–Si pairs. The most striking result of SiO_2 glass is the fact that each silicon is surrounded by four oxygens at a distance of about 1.6 Å. From the geometry of the tetrahedron, the distance and co-ordination number of oxygen–oxygen correlation are expected to be 2.65 Å and 6, respectively. The estimated values in Fig. 15 support these distributions. Further, the co-ordination number of Si–Si pairs is ~ 4. From this, we deduce that the fundamental unit of local nearest neighbour correlation in SiO_2 glass is the SiO_4 tetrahedral unit, but that the correlations of these units decay rapidly at the larger distance. In the case of Fe–P glass, the near neighbour correlation is interpreted as the superposition of the correlations of Fe–Fe and Fe–P pairs. Although these correlations are not necessarily resolvable, it is noticed that the number of near neighbours within a distance of 3.1 Å is about 13.4, and is close to 14 in crystalline Fe_3P [48]. This is in good agreement with the recent result of Logan [49], and this situation is also found in other metal–metalloid systems such as the Ni–P alloys of the previous section. Although the local ordering in both glasses at the near neighbour distance is tetrahedral, there is the following difference in detail between the structures of SiO_2 glass and Fe–P glass. As shown in the previous section, the structure of Fe–P glass can be expressed, to a first approximation, by randomly distributed Fe atoms like those of dense random packing model, in which the P atoms occupy the vacant space. In SiO_2 glass, the tetrahedral unit of SiO_4 is distinct, but the complete loss of correlation in these units arises at long range. In other words, the SiO_4 tetrahedral units are randomly distributed at a relatively lower density so as to construct the so-called random network structure. Fig. 16 shows a schematic diagram of

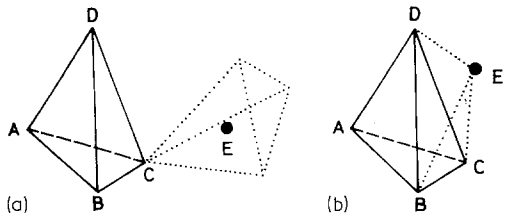

Figure 16 Schematic diagrams of the difference between the near neighbour distribution of atoms for an oxide glass (a) and that for a metallic glass (b).

this difference. Although the local ordering at the near neighbour distance is the tetrahedron in both glasses, the second nearest neighbour position E in oxide glass is larger than that in the case of metallic glasses. In metallic glasses the atoms are able to occupy the position E which is the centre of the triangle BCD in the side of the tetrahedron, but in oxide glasses, the atoms cannot occupy this position due to the covalent-like bonding Si–O–Si. We may further add that this inference is applicable to other oxide glasses and metallic glasses, from the results on glassy alkali metal silicates [47] and amorphous metals [1–8].

4. The crystallization behaviour of metallic glasses

4.1. Transformation sequence

The as quenched amorphous structure is in metastable state, and transformation to a stable crystalline phase should occur during heating above the characteristic "crystallization temperature" of a particular alloy. Although there have been a number of studies on the crystallization of various amorphous metals [1–3, 7], no general features have been made clear. From this point of view, the transformation sequences obtained in our work [31] are discussed below. During heating, the amorphous phase transforms progressively, rather than directly to a fully stable phase through a sequence of metastable phases. For instance [50], the transformation sequence in amorphous $Pd_{80}Si_{20}$ alloy has been identified as consisting of the following four successive stages; (1) the incipient stage of crystallization (Am′) during which some degree of ordering occurs in the atomic arrangements of the amorphous phase, (2) the appearance of a number of small Pd crystallites with a f c c structure within the amorphous matrix (MS-I), (3) the formation of a complex ordered metastable phase (MS-II) over the entire amorphous matrix with dispersed MS-I phase, and (4) the final stage to produce the stable phase (ST) consisting of Pd and Pd_3Si. It has been also found in this alloy that a prolonged annealing at the incipient stage of crystallization induces a change from amorphous phase to supersaturated metastable phase (SS) of a f c c microcrystalline assembly [7].

Similar transformation sequences have been observed for other amorphous alloys. The representative transformation sequence and the characteristics of the phases at each stage are summarized in Table V for five amorphous alloy systems.

In order to clarify the characteristics of transformation in detail, the time–temperature–transformation diagram of each metallic glass was constructed by using transmission electron micro-

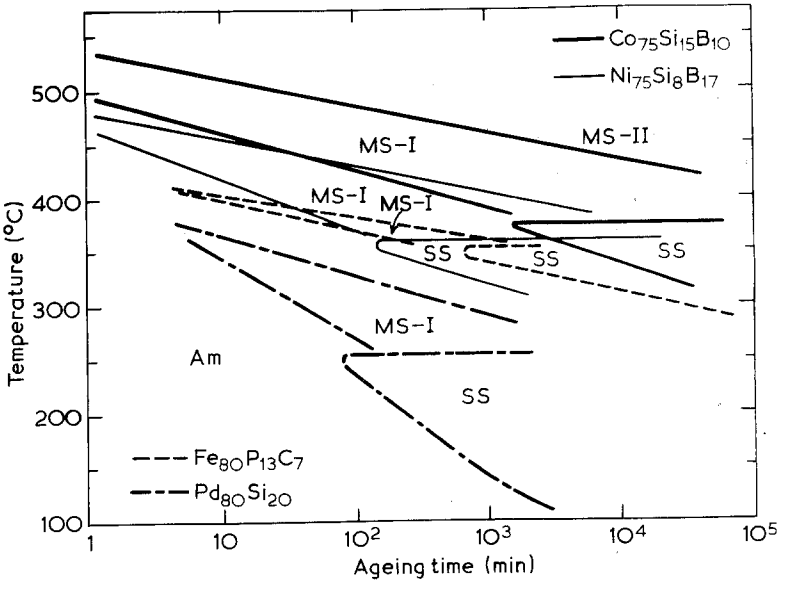

Figure 17 Time–temperature–transformation diagrams of four metallic glasses [31].

TABLE V Systematic transformation sequence of various amorphous metal–metalloid systems.

Phase	$Pd_{80}Si_{20}$	$Fe_{80}P_{13}C_7$	$Fe_{78}Si_{10}B_{12}$	$Co_{75}Si_{15}B_{10}$	$Ni_{75}Si_8B_{17}$
SS	fcc ($a = 3.912$ Å)	bcc ($a = 2.861$ Å)	bcc ($a = 2.848$ Å)	hcp ($a = 2.496$ Å) ($c = 4.041$ Å)	fcc ($a = 3.508$ Å)
MS-I	fcc ($a = 3.89$ Å)	bcc ($a = 2.87$ Å)	bcc ($a = 2.87$ Å)	hcp ($a = 2.51$ Å) ($c = 4.07$ Å)	fcc ($a = 3.52$ Å)
MS-11 . . . (Complex ordered phase?) . . .					
ST	Pd, Pd_3Si	Fe, Fe_3C Fe_3P	Fe, Fe_3Si Fe_{32}	Co, Co_3B Co_3Si	Ni, Ni_3B Ni_3Si
T_c(°C)*	380	410	505	480	482
T_c'(°C)†	250	350	–	375	360

*T_c: Crystallization temperature, at which the exothermic peak begins to appear at a scanning rate of 5°C min^{-1}.
†T_c': Critical temperature, below which the SS phase appears.

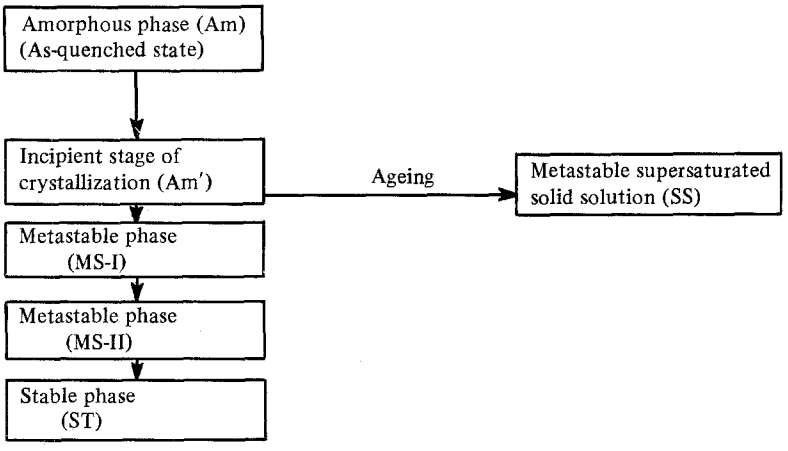

scopy, X-ray and electron diffraction methods. Fig. 17 illustrates the T–T–T curves of four metallic glasses, in which each phase corresponds to the respective crystallization sequence indicated in Table V. Although the transformation temperature of each alloy is different, the four metallic glasses show the same pattern of T–T–T curve. In addition, the following point is worthy of note in Fig. 17; a distinct difference in the transformation sequence is observable above and below the critical temperature, T_c'. For example, above this temperature crystallization proceeds through the two metastable phases and finally to the stable phase by nucleation and growth mechanisms. Below T_c', however, progressibe ageing changes the structure gradually from amorphous to single phase (SS). As seen in Table V, this phase has the same structure as that of the major metallic element, i.e. a fcc structure in Pd–base and Ni–base alloys, a bcc structure in Fe–base alloys and a hcp structure in Co–base alloys. These phases are highly stable after long ageing below the critical temperature and consist of an assembly of microcrystallites. Fig. 18 shows the transmission electron micrographs and electron diffraction patterns of the MS-I and SS phases after aging above and below T_c'. Although the two phases have the same crystal structure, the transformation mode is different; i.e. the MS-I phase precipitates within amorphous matrix by nucleation and growth mechanisms, while the SS phase grows gradually into an assembly of microcrystallites having diameters of about 50 to 100 Å over the entire matrix. Judging from the lattice parameter of these phases it is suggested that the former is a phase consisting of the nearly pure metallic

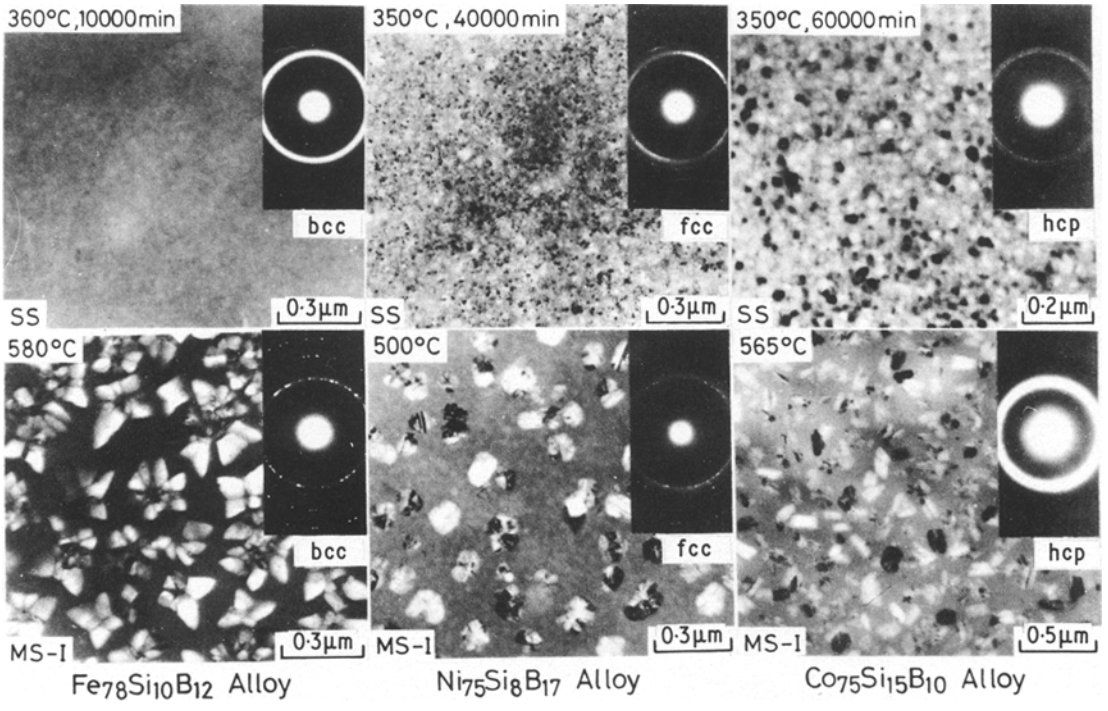

Figure 18 Electron micrographs of solid solution (SS) phase and metastable-I (MS-I) phase for Fe–Si–B, Ni–Si–B and Co–Si–B alloys [31].

element, and the latter is a supersaturated solid solution with the same composition as that of the matrix.

4.2. Thermal effects at lower temperature

It is essential to examine carefully the incipient stage of crystallization in order to understand the thermal instability of amorphous alloys. From this point of view, a detailed investigation of this stage was made using X-ray diffraction. Fig. 19 shows the structure factor and pair distribution function of Fe–P–C alloy aged for various times at 330° C [30]. A slight change is observed even within 1000 min; the first peak becomes sharper and the splitting of the second peak becomes less distinct. Upon further aging several new peaks superimpose on the original pattern of the amorphous phase, and these new peaks become continuously sharper with increasing ageing time. These data are quite similar to those for amorphous Pd–Si alloys [31]. The positions of the new peaks coincide with those of atoms in a b c c structure with a lattice parameter $a_0 = 2.86$ Å and are indicated by the vertical lines in Fig. 19. Of course the X-ray diffraction pattern for the sample aged for a long time exhibits the typical crystalline structure as shown in Fig. 20. These results are consistent with those of the electron microscopy. Similar behaviour due to short time annealing effect was found in other amorphous alloys [52]. In general, therefore, there are two stages in the structural changes brought about by ageing at lower temperatures. The initial stage corresponds to the incipient stage of crystallization (Am′), during which some degree of short range ordering occurs in the amorphous structure transforms to the single phase (SS) which has the same structure as the constituent metal. Although the precipitation mechanism of the single phase is not clear, it is proposed from X-ray and electron microscopic analyses that the crystallization takes place in the manner of continuous growth, that is, the short range ordered clusters which are prepared at the incipient stage of crystallization are gradually rearranged into a well-defined crystal structure without a long range diffusion of atoms.

In the recent studies [53–55], it has been found that some amorphous alloys have larger magnetic anisotropies and that the magnitude of these anisotropies is decreased by annealing at

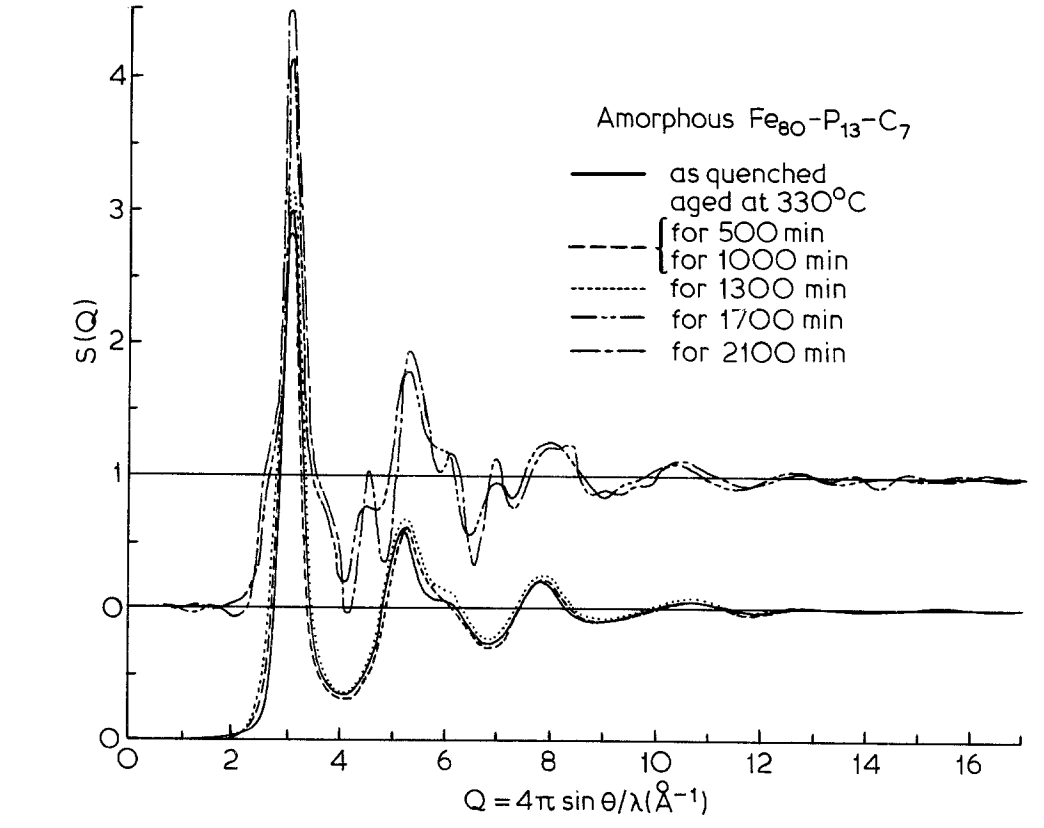

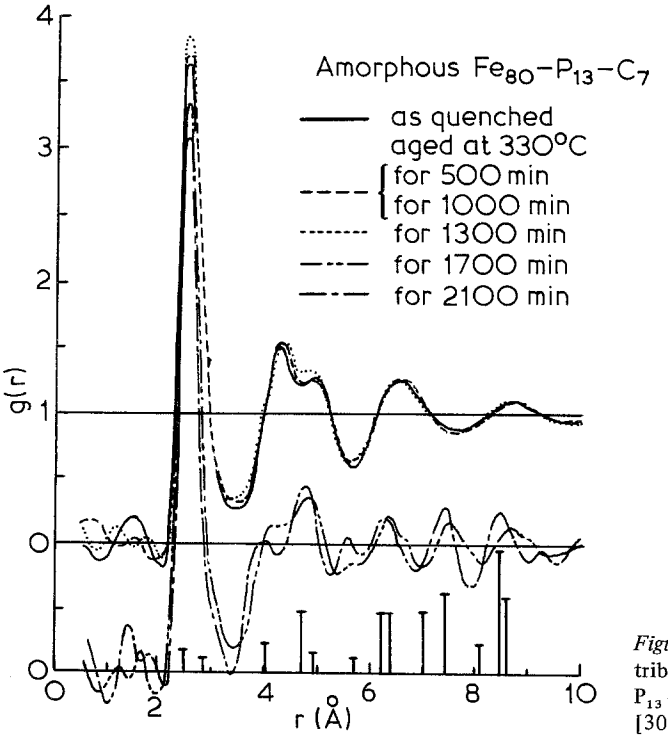

Figure 19 Interference function $S(Q)$ and pair distribution function $g(r)$ of an amorphous $Fe_{80}-P_{13}-C_7$ alloy aged at 330° C for various times [30].

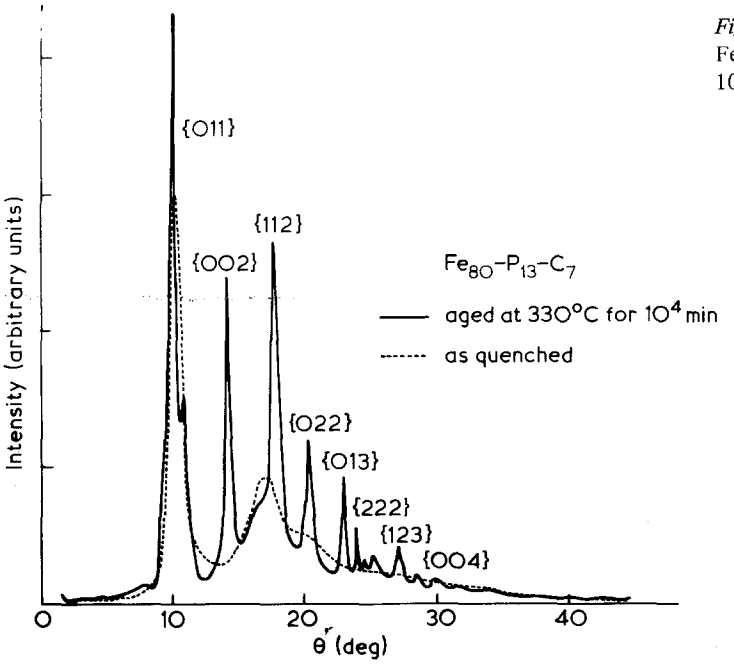

Figure 20 Intensity pattern of amorphous $Fe_{80}-P_{13}-C_7$ alloy aged at 330° C for 10^4 min [30].

temperatures too low to cause crystallization. The origin of this magnetic anisotropy is thought to involve anisotropies in short-range structural or compositional ordering [51] and/or internal strains arising from the rapid quenching [30, 53–55]. If these anisotropies or internal strains are present in the as-quenched specimen, they may be relaxed during annealing at the incipient stage of crystallization.

In order to clarify such annealing effects, the changes in various physical and mechanical properties have been examined with Pd–Si and Fe–P–C alloys aged at low temperatures [31]. These results are summarized in Fig. 21 together with the corresponding results for the disorder parameter ζ. The disorder parameter increases slightly, for example, with ageing time in the range of 30 to 200 min, then abruptly increases for ageing times greater than ~ 200 min, whereupon several peaks of a fcc structure appear on the X-ray diffraction pattern. In Fig. 21, at the incipient stage of crystallization (below ~ 200 min),

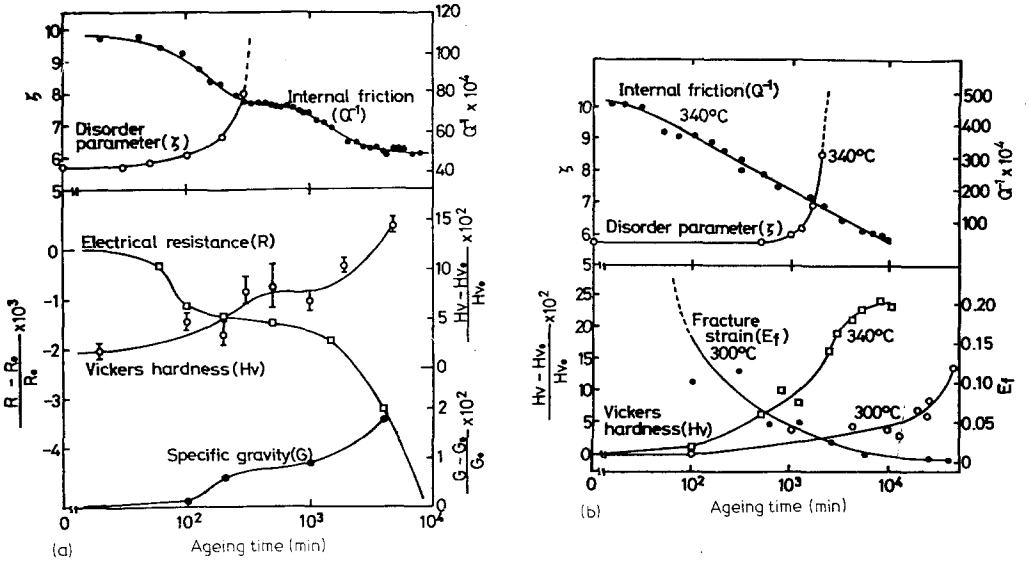

Figure 21 Changes in various properties of metallic glasses during ageing [31]; (a) $Pd_{80}-Si_{20}$ alloy aged at 200° C, (b) $Fe_{80}-P_{13}-C_7$ alloy aged at 330° C.

the internal friction and electrical resistance are decreased appreciably, while the specific gravity and microhardness are increased only slightly. Transformation of amorphous phase to the microcrystalline phase by further ageing treatments results in remarkable changes in all quantities. It is found that the former quantities are more sensitive to the atomic rearrangement in the short range order regime in comparison to the latter ones. Similar phenomena are also observed in the internal friction and hardness for Fe–P–C alloys as shown in Fig. 21. In these two figures it should be noticed, moreover, that the behaviour of fracture strain during ageing differs in these two alloys: in the Fe–P–C alloys a significant decrease of fracture strain occurs within very short times of the incipient stage, although in the Pd–Si alloys no change is detected even after long times during which crystallization clearly occurs.

The various experimental facts described above lead to the following conclusions. The ageing treatments at lower temperatures cause some short range ordering of atoms, resulting in the relaxation of internal strains or anisotropic configuration of atoms arising from the rapid quenching. Such atomic rearrangements are reflected in changes of the structure-sensitive properties such as electrical resistivity and internal friction. On the other hand, a remarkable decrease in the fracture strain of Fe–P–C alloys seem to be due to a change in the nature of the bonding between constituent atoms. The embrittlement after ageing treatments at lower temperatures is not a general character of all of amorphous metals and is perhaps characteristic to amorphous magnetic alloys. This is one of the interesting future problems.

4.3. Deformation effects

External stress is another important factor in determining the stability of the structure, and consideration of this problem will also be useful in discussing the mechanisms of deformation and fracture of amorphous alloys. Relevant experimental results obtained by X-ray analysis and electron microscopy are discussed below.

Fig. 22 shows the pair distribution function of Pd–Si alloys cold-rolled at two grades of reduction, 20 and 40% [7, 56, 57]. In this figure it is clearly seen that the height of the first peak decreases and the splitting of the second peak becomes less distinct. These results suggest that the deformation at room temperature produces a much more disordered atomic structure than that present in the as-quenched state. However, a specimen deformed by cold rolling does not undergo homogeneous deformation. Accordingly, X-ray data may consist of a mixture of two kinds of diffraction from deformed and undeformed parts. To avoid this, direct observation using an electron microscope (1000 kV) was performed using a thin foil prepared by electrolytic polishing of the cold-rolled specimen [57]. Fig. 23 shows a transmission electron micrograph together with the intensity curves of a selected area electron diffraction pattern from the regions labelled A and B. Several bands with a bright contrast are observed and the

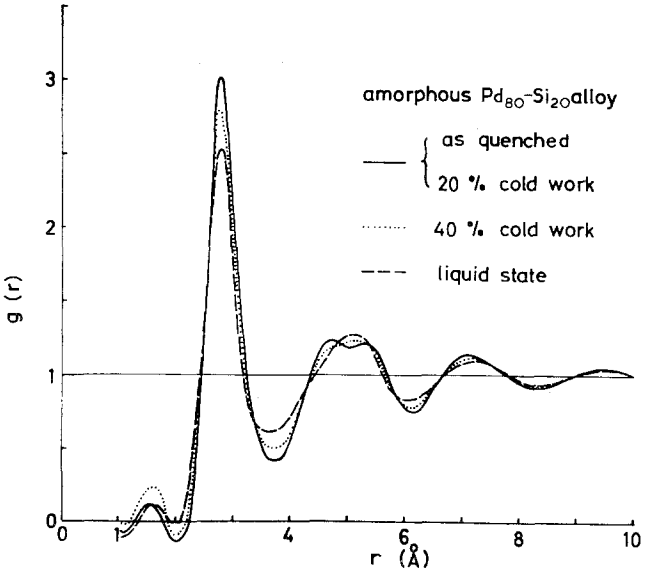

Figure 22 Pair distribution function $g(r)$ of cold-rolled $Pd_{80}-Si_{20}$ alloy [57].

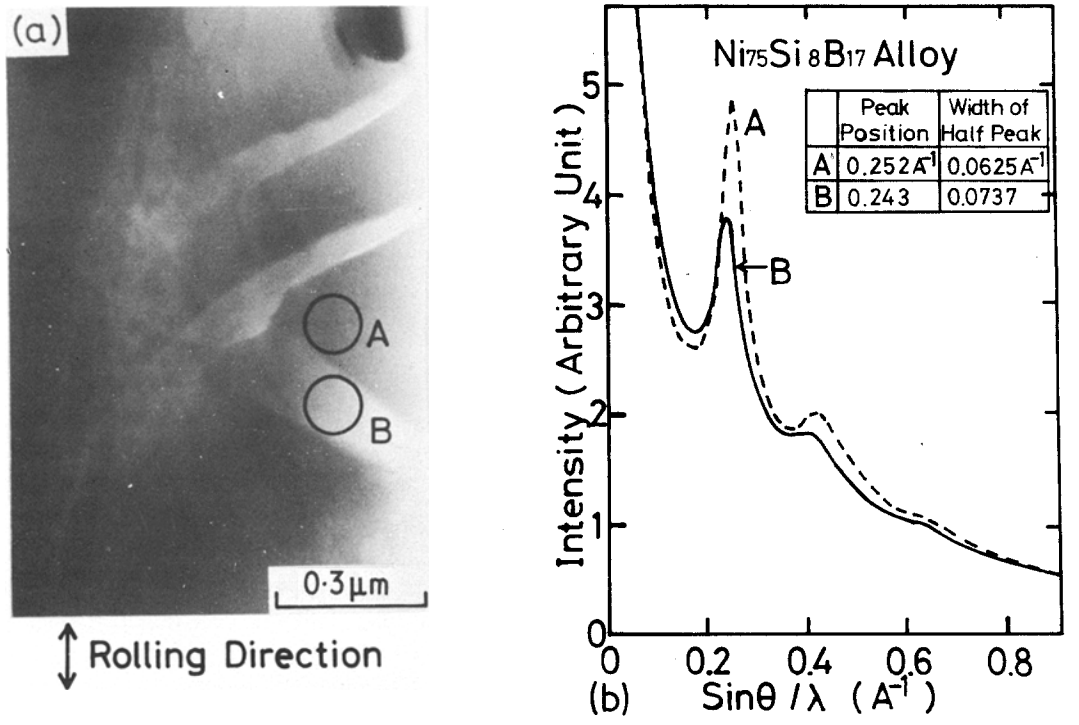

Figure 23 Deformation bands in Ni_{75}–Si_8–B_{17} metallic glass cold-rolled to 25% reduction [57].

diffraction pattern from such as this region (B) illustrates that the structure within the bright band is in a much more disordered state than that of the darker contrast region (A). A similar result is reported using positron annihilation techniques [58, 59]. Although the reason for the appearance of this bright contrast is unknown, it is possible that the band is induced by deformation. No detailed discussion of the effect of deformation is available at the present time.

4.4. Alloying effects on thermal stability

Amorphous iron-based alloys quenched from the liquid state have high static strength, consistently high toughness and good resistance to chemical and pitting corrosion [7, 60]. It is thus important to clarify the effect of alloying elements on the thermal stabilities of amorphous metals. There are a few studies of this kind [61–63], and the available results for amorphous iron-based alloys are considered below. Fig. 24a shows the relationship between the crystallization temperature and the concentration of alloying elements [63]. Generally, the crystallization temperatures decrease when the atomic number of an alloying element is greater than that of iron, and increases when it is smaller.

According to Hume–Rothery the prime factors in determining the properties of alloys are relative atomic size, electronegativity and valency. In the following discussion, consideration is given to the role these factors play in determining the properties of amorphous iron-based alloys. First, the atomic size is considered to be less important in determining the mechanical strength and thermal stability of the alloys, since they show the addition of Cr and Ni alter the crystallization temperatures of the alloys in distinct and opposite ways, although the atomic diameters of these elements are nearly equal (2.37, 2.34 and 2.31 Å for Cr, Fe and Ni, respectively). The atomic sizes of the alloying elements differ from that of iron by not more than 15%, and the Hume–Rothery's 15% size factor rule seems to be applicable to the present amorphous iron-based alloys. Consequently effects of alloying elements are thought to be insignificant in modifying the random structure of amorphous iron-based alloys as far as the atomic size effect is concerned. Secondly, by similar reasoning, the electronegativity has little or no effect in determining the crystallization temperature of amorphous iron-based alloys. The electronegativity of Fe, Co and Ni is given by Pauling [64] as 1.8 for each element, but, alloying gives

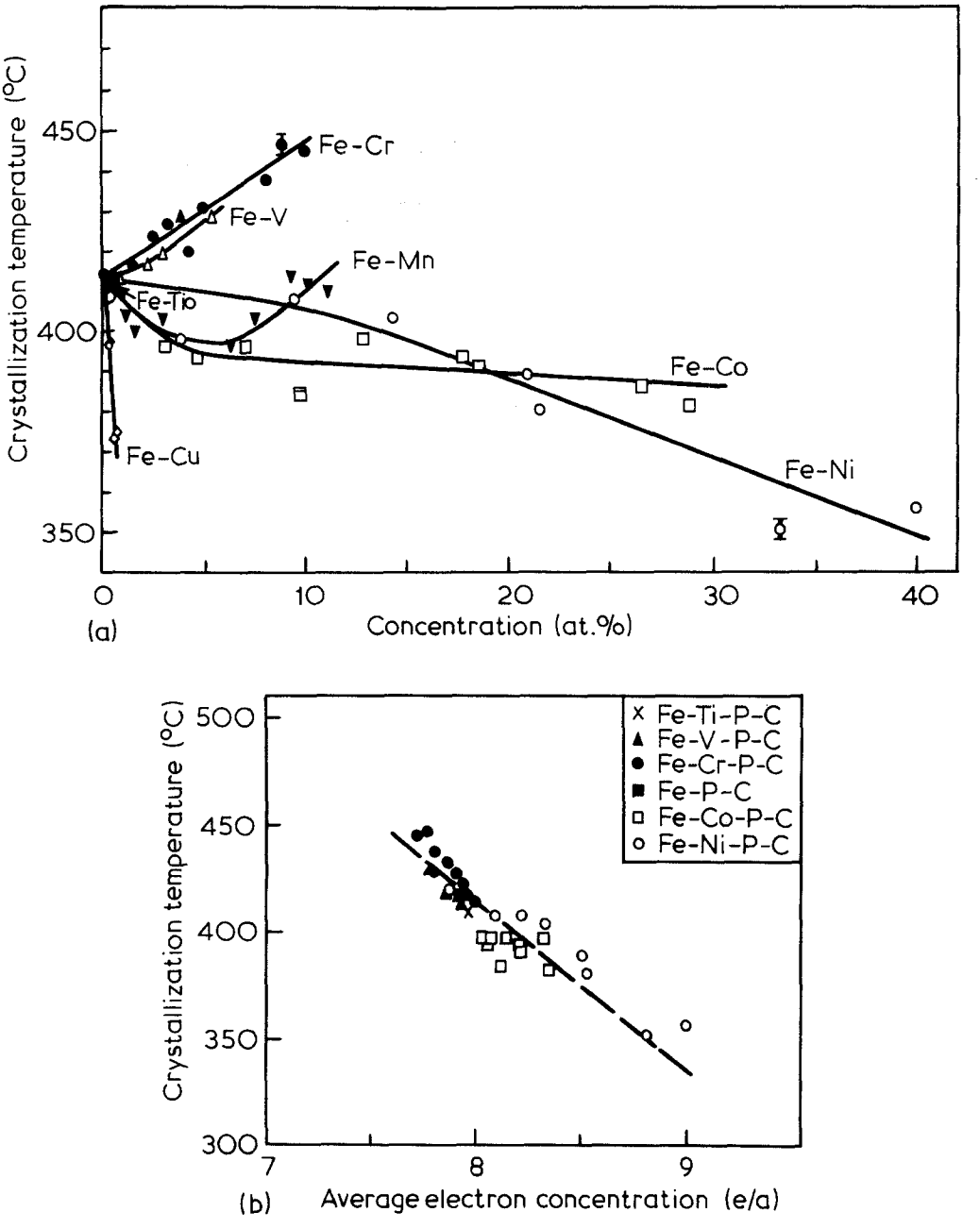

Figure 24 Effect of alloying elements on the crystallization temperature of amorphous iron-based alloys [63].

rise to significant changes in the crystallization temperature. Therefore this also cannot be a major factor in determining the magnitude of the crystallization temperature.

Following the above arguments the factor yet to be considered is the relative valence of alloying elements. In Fig. 24b the measured values of the crystallization temperatures of the amorphous iron-based alloys are plotted as a function of the averaged outer-electron concentration of metallic atoms (e/a), which is taken as a measure of the valency of transition elements in alloys. By taking the numbers of the outer electrons (s and d shells) to be from 4 to 10 for Ti to Ni, respectively, the average concentrations were obtained by the weighted means according to the atomic percentage of the transition elements. Manganese, which often exhibits anomalous features in crystals, is omitted

from this analysis. It is clearly seen from this figure that the crystallization temperatures vary almost linearly with $1/(e/a)$. This gives qualitative support for the suggestion that bonding plays a significant role in the thermal stability of these amorphous alloys, and that the partial bonds are formed by the overlap of the s–p hybrid orbitals of P or C atoms and the s–p–d orbitals of 3d transition metals such as Fe. Since a linear relationship between microhardness and crystallization temperature has also been established [63], there seems to be many stimulating topics in this field. However, no definite conclusions can be drawn concerning the alloying effects at the present time.

5. Concluding remarks

The recent progress in the study of metallic glasses reveals much about their characteristic structure, including their difference from liquid structures or from oxide glass structures. The structure of a metallic glass seems to be best described by the topological disorder model, the so-called dense random packing model, first suggested for liquids by Bernal [65]. There are many unsolved problems concerning metallic glasses such as the crystallization process and the formation of amorphous phases in general. A detailed study of several effects on the thermal instability of amorphous phases such as those of thermal, deformation and alloying, may be one way to clarify these problems. As is shown in Section 3.3, the size factor difference of more than 15% in transition metal–metalloid systems such as Ni–P alloys, seems to be related to the formation and composition range of metallic glasses, as well as to the bonding effect between atoms. But there is a need for further experiments and consideration before firm conclusions can be arrived at.

Acknowledgments

The authors are grateful for valuable discussion with Professor S. Tamaki. We are also indebted to Professors M. Ohtani and Y. Shiraishi for their support and encouragement in this study. One of us (YW) wishes to thank Professors C. N. J. Wagner and T. Egami and Drs G. S. Cargill III, T. Ichikawa and A. Inoue for communicating their results and for useful comments and also expresses thanks to the Sakkokai Foundation and Hattori Hohkohkai for the provision of grants.

References

1. B. S. GIEESEN and C. N. J. WAGNER, in "Liquid Metals" edited by S. Z. Beer (Marcel Dekker, New York, 1972) p. 633.
2. H. JONES, *Rep. Progr. Phys.* **36** (1973) 1425.
3. H. JONES and C. SURYANARYANA, *J. Mater. Sci.* **8** (1973) 705.
4. C. V. GOKULARATHNAM, *ibid* **9** (1974) 673.
5. G. S. CARGILL III, in "Solid State Physics" edited by F. Seitz, D. Turnbull and H. Erenreich, Vol. 30 (Academic Press, New York, 1975) p. 227.
6. Y. WASEDA, *J. Solid State Phys. (Japan)* **10** (1975) 459.
7. T. MASUMOTO and R. MADDIN, *Mater. Sci. Eng.* **19** (1975) 1.
8. S. TAKAYAMA, *J. Mater. Sci.* **11** (1976) 164.
9. J. BLETRY and J. F. SADOC, *J. Phys. F: Metal Phys.* **5** (1975) L110.
10. W. P. O'LEARY, *ibid* **5** (1975) L175.
11. J. F. SADOC and J. DIXMIER, *Mater. Sci. Eng.* **23** (1976) 187.
12. Y. WASEDA and S. TAMAKI, *Z. Physik* **B23** (1976) 315.
13. Y. WASEDA, H. OKAZAKI, M. NAKA and T. MASUMOTO, *Sci. Rep. Res. Inst. Tohoku Univ.* **26A** (1976) 12.
14. J. G. RAMESH and S. RAMASESHAN, *J. Phys. C: Solid State Phys.* **4** (1971) 3029.
15. S. RAMASESHAN and S. C. ABRAHAMS, "Anomalous Scattering" (International Union of Crystallography, Amsterdam, 1975) p. 139.
16. Y. WASEDA and S. TAMAKI, *Phil. Mag.* **32** (1975) 951.
17. J. E. ENDERBY, D. M. NORTH and P. A. ENGELSTAFF, *ibid* **14** (1966) 961.
18. R. W. JAMES, "The Optical Principles of the Diffraction of X-rays", (Bell, London, 1948).
19. D. T. CROMER, *Acta Cryst.* **18** (1965) 17.
20. *Idem, ibid* **A32** (1976) 339.
21. T. ICHIKAWA, *Phys. Stat. Sol. (a)* **19** (1973) 707.
22. Y. WASEDA and S. TAMAKI, *Phil. Mag.* **32** (1975) 273.
23. L. B. DAVIES and P. J. GRUNDY, *Phys. Stat. Sol. (a)* **8** (1971), 189.
24. H. A. DAVIES, *Phys. Chem. Glasses* **17** (1976) 159.
25. P. K. LEUNG and J. G. WRIGHT, *Phil. Mag.* **30** (1974) 995.
26. H. S. CHEN and B. K. PARK, *Acta Met.* **21** (1973) 395.
27. C. N. J. WAGNER, T. B. LIGHT, N. C. HALDER and W. E. KUKENS, *J. Appl. Phys.* **39** (1968) 3690.
28. T. ICHIKAWA, *Phys. Stat. Sol. (a)* **29** (1975) 293.
29. G. S. CARGILL III and S. KIRKPATRIK, International Conference on Structure and Excitation of Amorphous Solids, Williamsburg, March (1976), (AIP, New York, 1977).
30. Y. WASEDA and T. MASUMOTO, *Z. Physik* **B22** (1975) 121.
31. T. MASUMOTO, Y. WASEDA, H. KIMURA and A. INOUE, *Sci. Rep. Res. Inst. Tohoku Univ.* **26A** (1976) 21.

32. Y. WASEDA, H. OKAZAKI and T. MASUMOTO, Proceedings of International Conference on the Structure of Non-Crystalline Mateirals, Cambridge, 1976 (Taylor and Francis, London, 1977).
33. Y. WASEDA, T. MASUMOTO and S. TAMAKI, Proceedings of 3rd International Conference on Liquid Metals, Bristol, 1976 (Institute of Physics, London, 1977).
34. C. FINBAK, *Acta Chem. Scand.* **3** (1949) 1279.
35. T. MORIMOTO, *Sci. Rep. Res. Inst. Tohoku Univ.* **A3** (1951) 39.
36. S. RUNDQUIST, E. HASSLER and LUNDVIC, *Acta Chem. Scand.* **16** (1962) 242.
37. G. S. CARGILL III and R. W. COCHRANE, *J. de Physique Coll. Suppl.* **5** (1974) C4-269.
38. Y. WASEDA, *Bull. Japan. Institute of Metals* **15** (1976) 167.
39. P. MRAFKO and P. DUHAJ, *Phys. Stat. Sol. (a)* **22** (1974) 151.
40. K. SUZUKI, T. FUKUNAGA, M. MISAWA and T. MASUMOTO, *Mater. Sci. Eng.* **23** (1976) 215.
41. Y. WASEDA, Proceedings of 3rd International Conference on Liquid Metals, Bristol, 1976 (Institute of Physics, London, 1977).
42. C. D. THOMAS and N. S. GINGRICH, *J. Chem. Phys.* **6** (1938) 659.
43. Y. WASEDA and M. OHTANI, *Z. Physik* **B21** (1975) 229.
44. W. E. LUKENS and C. N. J. WAGNER, *J. Appl. Cryst.* **9** (1976) 159.
45. M. L. MOZZI and B. E. WARREN, *ibid* **2** (1969) 164.
46. A. H. NARTEN, *J. Chem. Phys.* **56** (1972) 1905.
47. Y. WASEDA and H. SUITO, *Tetsu to Hagane* **62** (1976) 1675.
48. S. RUNDQUIST, *Acta Chem. Scand.* **16** (1962) 1.
49. J. LOGAN, *Phys. Stat. Sol. (a)* **32** (1975) 361.
50. T. MASUMOTO and R. MADDIN, *Acta Met.* **19** (1971) 725.
51. G. C. CHI and G. S. CARGILL III, *Mater. Sci. Eng.* **23** (1976) 155.
52. T. EGAMI and T. ICHIKAWA, private communication (August, 1976).
53. H. FUJIMORI, T. MASUMOTO, Y. OBI and M. KIKUCHI, *Japan J. Appl. Phys.* **13** (1974) 1889.
54. T. EGAMI, P. J. FLANDERS and C. D. GRAHAM Jr., *AIP Conf. Proc.* **24** (1975) 697.
55. F. E. LUBORSKY, J. J. BECKER and R. O. McCARY, *Trans. on Magnetics* (1975) in press; (Technical Information Series of GE, No. 75CRD134 (1975)).
56. T. MASUMOTO and M. KOIWA, Abstracts of Meeting of Japan Institute of Metals, Fukuoka, 1973 (Japan Inst. Metals, Sendai, 1973) p. 246.
57. T. MASUMOTO, H. KIMURA, A. INOUE and Y. WASEDA, *Mater. Sci. Eng.* **23** (1976) 141.
58. H. S. CHEN and S. Y. CHUANG, *Appl. Phys. Lett.* **27** (1975) 316.
59. H. S. CHEN, *Scripta Met.* **9** (1975) 411.
60. K. HASHIMOTO, M. NAKA and T. MASUMOTO, *Sci. Rep. Res. Inst. Tohoku Univ.* **26A** (1976) 49.
61. D. E. POLK and H. S. CHEN, *J. Non-Cryst. Solids* **15** (1974) 165.
62. H. S. CHEN, *Acta Met.* **22** (1974) 1505.
63. M. NAKA, S. TOMIZAWA, T. WATANABE and T. MASUMOTO, Proceedings of 2nd International Conference on Rapidly Quenched Metals, Boston, Mass. (1975) (MIT Press, Boston, 1977).
L. PAULING, "The Nature of the Chemical Bond", (Cornell Univ. Press, New York, 1960).
65. J. D. BERNAL, *Nature* **183** (1959) 141.
66. K. FURKUKAWA, *Sci. Rep. Res. Inst. Tohoku Univ.* **A12** (1960) 368.

Received 28 January and accepted 14 March 1977.